SAND2022-14059J

# Laser-Driven Ionization Mechanisms of Aluminum for Single Particle Aerosol Mass Spectrometry

Amanda M. Lietz[1,†*], Benjamin T. Yee[1,‡], Jeffrey Musk II[1], Harry K. Moffat[1], Dora K. Wiemann[1], Taylor Settecerri[1], David Fergenson[2], Michael A. Omana[1], and Matthew M. Hopkins[1]

[1] Sandia National Laboratories, 1515 Eubank Blvd. SE, Albuquerque, NM 87123, USA

[2] Livermore Instruments, 2038 Livingston St. Suite B, Oakland, CA 94606, USA

[†] Present address: North Carolina State University Department of Nuclear Engineering, 2500 Stinson Dr., Raleigh, NC 27695, USA

[‡] Present address: Lam Research Corporation, 11155 SW Leveton Dr., Tualatin, OR 97062, USA

[*] Author to whom correspondence should be addressed: alietz@ncsu.edu

Single particle aerosol mass spectrometry (SPAMS), an analytical technique for measuring the size and composition of individual micron-scale particles, is capable of analyzing atmospheric pollutants and bioaerosols much more efficiently and with more detail than conventional methods which require the collection of particles onto filters for analysis in the laboratory. Despite SPAMS' demonstrated capabilities, the primary mechanisms of ionization are not fully understood, which creates challenges in optimizing and interpreting SPAMS signals. In this paper, we present a well-stirred reactor model for the reactions involved with the laser-induced vaporization and ionization of an individual particle. The SPAMS conditions modeled in this paper include a 248 nm laser which is pulsed for 8 ns to vaporize and ionize each particle in vacuum. The ionization of 1 μm, spherical Al particles was studied by approximating them with a 0-dimensional plasma chemistry model. The primary mechanism of absorption of the 248 nm photons was pressure-broadened direct photoexcitation to Al($y^2D$). Atoms in this highly excited state then undergo superelastic collisions with electrons, heating the electrons and populating the lower energy excited states. We found that the primary ionization mechanism is electron impact ionization of various excited state Al atoms, especially Al($y^2D$). Because the gas expands rapidly into vacuum, its temperature decreases rapidly. The rate of three-body recombination ($e^- + e^- + Al^+ \rightarrow Al + e^-$) increases at low temperature, and most of the electrons and ions produced recombine within several μs of the laser pulse. The importance of the direct photoexcitation indicates that the relative peak heights of different elements in SPAMS mass spectra may be sensitive to the available photoexcitation transitions. The effects of laser intensity, particle diameter, and expansion dynamics are also discussed.

Keywords: aerosol mass spectrometry, plasma modeling, laser-produced plasmas, laser desorption ionization

## I. Introduction

Single particle aerosol mass spectrometry (SPAMS) is a sensitive technique for determining the sizes and chemical compositions of individual aerosol particles. The technique is particularly useful for measurements in the atmosphere, where particles can influence precipitation or produce negative health impacts [1, 2]. Mass spectrometry has provided critical data for many recent insights related to atmospheric aerosols [2]. By ionizing one particle at a time, SPAMS can provide a mass spectrum and size for each particle, rather than an average over many particles. This information is valuable because the particles in the atmosphere come from a variety of sources, both natural and anthropogenic. SPAMS has therefore been used in many recent studies of atmospheric particles. (Though several devices with various designs have been developed and given unique names, for simplicity we refer to any device that performs single particle aerosol mass spectrometry as a SPAMS system.) For example, Yang *et al*. used SPAMS to analyze the particles present in an urban tunnel [3]. With an artificial neural network, the particles were divided into categories and attributed to different sources such as coal combustion and vehicle exhaust. Ault *et al*. used SPAMS to characterize atmospheric particles in the Sierra Nevada mountains in the United States which are critical to precipitation and to California's water supply [4]. Because single particle spectra were obtained, it was possible to attribute a fraction of the particles to dust originating in Asia.

Though many SPAMS systems have been developed and used, the quantitative interpretation of the spectra has been limited by the lack of a validated model of the ionization process. For example, a linear response between signal strength and concentration would be ideal but has not always been observed [5, 6]. To understand the opportunities and limitations for quantitative analysis, the ionization mechanisms must be better understood. Understanding the primary mechanisms of ionization will also enable more informed design choices for SPAMS systems. Reducing the size and weight of SPAMS systems would make them more practical to test aerosols on a vehicle or aircraft [7]. Testing in the field would eliminate the impact of storage and filter interactions on the particle chemistry [8].

Several authors have discussed the ionization mechanisms in SPAMS devices which rely on laser desorption ionization. Reinard and Johnston used covariance mapping in a SPAMS system to investigate the ionization mechanisms [9]. With a 193 nm laser and particles 50-220 nm in size with varying compositions, the authors concluded that the atoms and molecules first formed cations, free electrons and neutrals, then electron attachment gave rise to anions. When expansion occurs more rapidly, fewer anions are formed and there is less charge exchange amongst the positive ions. Reducing charge exchange is desirable because it preserves the signal from less energetically favorable ions (i.e. ions with a higher ionization energy).

Murphy summarized the design guidelines for SPAMS devices, including a discussion of the ionization mechanisms [7]. Though it is unclear what the primary ionization mechanisms are, some explanations were eliminated. The review asserts that it does *not* appear to be single photon ionization, resonance enhanced multiphoton ionization (REMPI), "plasma formation" (though it is not clear which microscopic ionization process this refers to), or thermal ionization. Murphy concluded that the more likely ionization mechanisms involve photoionization of excited states or multiphoton ionization, which may be enhanced by clusters. Oh *et al*. discussed the potential ionization mechanisms for 532 nm ionization laser and concluded that electron impact ionization is most likely the dominant ionization mechanism, with electron heating through inverse Bremsstrahlung [10].

Though SPAMS is the technology of interest in this study, laser vaporization and ionization have also been used and modeled for many other applications. In laser-induced breakdown spectroscopy (LIBS), typically one or two laser pulses are used to ionize solid or liquid samples [11]. The resulting optical emission spectra are analyzed to determine the chemical composition of the sample. This analysis is often simpler if the plasma is in local thermodynamic equilibrium (LTE) while the spectrum is collected. In LIBS, spectra are typically taken several hundred ns after the laser pulse, after the continuum emission has decreased. Though LIBS typically uses a higher laser energy than a SPAMS system, and often achieves multiply ionized species, many of the investigations and modeling techniques are also useful in this application. One critical difference is that SPAMS systems typically ionize samples in vacuum, whereas in LIBS the background pressure is usually much higher.

Several experimental studies provide some background on expected temperatures and behaviors in these systems. Shakeel *et al*. measured the electron temperature and density of a Ge plasma produced in a LIBS system with a 1064 nm laser [12]. Electron temperatures of 6,500 to 14,000 K were observed, and electron densities were typically near $8 \times 10^{17}$ $cm^{-3}$. When the background gas pressure was reduced (as low as 6 Torr), the plasma was able to expand faster, resulting in a lower temperature. Shaikh *et al*. also measured the electron temperature and density of an Al LIBS plasma at several laser wavelengths [13]. At 1064 nm most of the energy deposition was due to inverse Bremsstrahlung, while at shorter wavelengths such as 355 nm, most of the energy was deposited by photoionization of electronically excited Al atoms. As a result, the electron temperature was higher for a 1064 nm laser, but the electron density was larger for a 355 nm laser. Lu *et al*. performed experimental measurements of electron temperature and density (assuming LTE) in an Al plasma produced with a 248 nm laser [14]. The laser intensity was similar to that of the SPAMS device studied here, and the electron temperature was lower for a lower background pressure (as low as 10 Torr) because the Al could expand more rapidly.

Morel *et al*. modeled Al plasma formation in a LIBS system using a 0-dimensional approach, where the plasma is approximated as a well-stirred reactor. They expanded upon this work using a multi-region model [15, 16]. They showed that for ns laser pulses, inverse Bremsstrahlung caused heating of the electrons resulting in electron-impact excitation and ionization. For ultrafast laser pulses however, inverse Bremsstrahlung was not significant, and the electron temperature tends to be equal to the gas temperature. However, ultrafast laser pulses have also been explored for SPAMS, and Zawadowicz *et al*. argued that the ionization mechanisms may be similar to that of nanosecond pulses [17]. Colonna *et al*. modeled the expansion of a titanium LIBS plasma into oxygen with a reactive 1-dimensional fluid model and showed that the expansion dynamics were sensitive to the background pressure [18]. Colonna *et al*. later demonstrated a significant vibrational nonequilibrium in two-dimensional fluid modeling of a LIBS plasma expanding into nitrogen [19].

In this paper, a new model describing the evolution of neutral and charged species encountered in a SPAMS system is presented. The model is applied to spherical Al particles 0.4 – 8 μm in diameter exposed to an 8 mJ, 8 ns pulse from 248 nm laser. The non-equilibrium plasma dynamics are modeled using a two-temperature 0-dimensional plasma chemistry model. Focusing on pure Al particles enables more detailed modeling than would be possible with more chemically complex particles and provides insights on measurements of harmful metal-containing atmospheric particles [20]. The device and model descriptions appear in Sec. II. The modeling results are discussed in Sec. III, including the chemistry and ionization mechanisms. The effect of laser energy, particle diameter, and expansion rate are also discussed. Concluding remarks and implications for SPAMS design appear in Sec. IV. An improved understanding of the ionization processes in SPAMS on this model system will enable more informed design choices that could improve the size, weight and power requirements for use in the field, as well as more accurate interpretation of SPAMS data.

## II. Model Description

### A. SPAMS Setup

Though this work is focused on modeling, the conditions selected are based on those of the SPAMS 3.0 Instrument by Livermore Instruments, Inc., shown schematically in Fig. 1. A SPAMS 3.0 consists of an aerodynamic lens system which focuses particles into a stream which is directed into a vacuum chamber (~$10^{-6}$ Torr during operation). A continuous wave 405 nm laser is used to monitor this stream and triggers an ionization laser to fire (after a 3 μs delay) when a particle with a diameter greater than 100 nm passes through it. Once the laser is triggered, an 8 mJ, 248 nm pulse ionizes the particle, and the resulting ions are collected by opposing time-of-flight mass spectrometers. The laser pulse has a full-width half maximum (FWHM) duration of 8 ns, and the beam size was focused to 1 mm by 0.5 mm where it intersects the particle flight path. These parameters resulted in a peak laser intensity of $1.9 \times 10^8$ W/cm$^2$ and a fluence of 1.6 J/cm$^2$.

**B. Global Modeling**

To quantify the excitation and ionization dynamics, a 0-dimensional, well-stirred reactor approach was used to represent the plasma. The control volume is the volume containing the Al vapor which was vaporized from the particle, and it is approximated as spherical. The density of electrons is calculated by

$$\frac{dn_e}{dt} = \sum_j^{rxns} \left(a_{e,j}^{RHS} - a_{e,j}^{LHS}\right) R_j - \frac{A}{V}\Gamma_{e,diff} - \frac{n_e}{V}\frac{dV}{dt} \#(1)$$

where $n_e$ is the number density of electrons. The first term on the right-hand side accounts for reactions within the control volume, and the second term accounts for diffusion losses of electrons as they escape the control volume into the surrounding vacuum. The third term accounts for expansion of the control volume as a function of time. $a_{e,j}^{RHS}$ and $a_{e,j}^{LHS}$ are the product and reactant stoichiometric coefficients for electrons in reaction $j$. $V$ is the volume of the expanding particle material, and $A$ is the surface area of the control volume. $\frac{dV}{dt}$ is based on an estimate of expansion dynamics to be described in Sec. B.2. For simplicity, we have not noted the time-dependence explicitly in this model description, but all variables on the right-hand side of Eq. 1 are time-dependent, except the stoichiometric coefficients (e.g. $R_j(t)$, $A(t)$, $\Gamma_{e,diff}(t)$). $R_j$ is the rate for the single-directional reaction $j$ calculated by the expression,

$$R_j = k_j \prod_i^{LHS} n_i \,, \#(2)$$

where $k_j$ is the reaction rate coefficient, which can be provided in Arrhenius form or result from integrating a cross section over a Maxwellian distribution function. For example, for the reaction $e^- + Al \rightarrow Al^+ + e^- +$

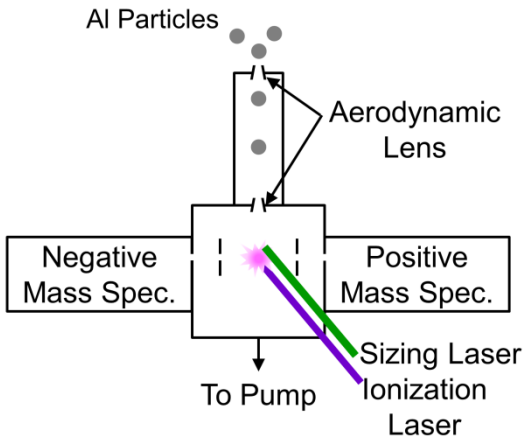


Figure 1. A simplified schematic of SPAMS 3.0 developed by Livermore Instruments, Inc. Particles are introduced at atmospheric pressure, and the pressure decreases across the aerodynamic lens. Two time-of-flight mass-spectrometers are used to collect the positive and negative ions.

$e^-$ with a rate of $k_{iz}$, $a_e^{RHS} = 2$ and $a_e^{LHS} = 1$, and the first term in Eq. 1 would be $(2-1)k_{iz}n_e n_{Al}$. The assumption of a Maxwellian electron distribution is expected to be valid in the early timescales of expansion when the collision rates are high, but its accuracy may decrease during the expansion. $n_i$ is the density of reactant *i*. In the case of photoionization reactions,

$$R_j = \sigma_j \phi^m \prod_i^{LHS} n_i \text{ ,\#(3)}$$

Where $\sigma_j$ is the cross section of reaction *j* and $\phi$ is the flux of photons. $m$ = 1 for single-photon processes, and $m$ = 2 for two-photon processes. When $m$ > 1, the units of the cross section are modified such that $R_j$ has units of $cm^{-3}s^{-1}$. The diffusion flux of electrons, $\Gamma_{e,diff}$, is calculated by

$$\Gamma_{e,diff} = \frac{n_e}{4}\sqrt{\frac{8k_B T_e}{\pi m_e}}\exp\left(-\frac{e\Phi_{plasma}}{k_B T_e}\right) \text{\#(4)}$$

where $k_B$ is Boltzmann's constant, $T_e$ is the electron temperature, $m_e$ is the electron mass, and $e$ is the elementary charge. The factor before the exponential in Eq. 4 represents the thermal flux of electrons into the sheath of the expanding plasma, and the exponential represents the fraction of electrons with sufficient energy to transit the sheath and escape the plasma [21]. $\Phi_{plasma}$ is the plasma potential, which is calculated from the total space charge in the plasma volume:

$$\Phi_{plasma} = \frac{Q}{4\pi\varepsilon_0 r} = \frac{\sum_i^{species} q_i n_i}{4\pi\varepsilon_0 r} V \text{,\#(5)}$$

where the sum is over all species, $q_i$ is the charge of species *i* in Coulombs, and *r* is the radius of the control volume (assuming a spherical volume). While including diffusion of electrons has a minor impact in this case, it enables the model to address the limit in which a low ion density may be insufficient to retain the electrons.

The rate of change of the densities of other species has a similar form to that of electrons:

$$\frac{dn_i}{dt} = \sum_j^{rxns}\left(a_{i,j}^{RHS} - a_{i,j}^{LHS}\right)R_j - \frac{n_i}{V}\frac{dV}{dt} \text{\#(6)}$$

where $n_i$ refers to the number density of species *i*.

A two-temperature model is used throughout, where the electrons have their own temperature, $T_e$, while all other neutrals and ions are assumed to share the common gas temperature, $T_g$. Both $T_e$ and $T_g$ are determined using their own energy equation. For the electron energy equation,

$$\frac{d\left(\frac{3}{2}k_B n_e T_e\right)}{dt} = P_{Ohmic} + \sum_j^{rxns}\Delta\epsilon_{e,j}R_j - \frac{A}{V}\left(\frac{3}{2}k_B T_e\right)\Gamma_{e,diff} - \gamma\frac{\left(\frac{3}{2}k_B n_e T_e\right)}{V}\frac{dV}{dt} \text{,\#(7)}$$

where $P_{Ohmic}$ is the power density transferred to electrons by Ohmic heating due to the oscillating electric field of the laser. $\Delta\varepsilon_{e,j}$ is the change in electron energy from reaction *j*, and $\gamma$= 5/3, for isentropic expansion of the electron gas. The Ohmic heating is calculated by

$$P_{Ohmic} = \frac{e^2 n_e E_{laser}^2 \nu_m^2}{2m_e\left(\omega_{laser}^2 + \nu_m^2\right)} \text{,\#(8)}$$

where $E_{laser}$ is the time-dependent magnitude of electric field of the laser, $\omega_{laser}$ is the angular frequency of the laser, and $\nu_m$ is the momentum transfer collision frequency, calculated from the elastic scattering cross section using the method from Surendra *et al.* [22]. The electric field of the laser is calculated from the photon flux

$$E_{laser} = \sqrt{\frac{h\omega_{laser}}{\pi\varepsilon_0 c}\phi} \text{.\#(9)}$$

where $h$ is Planck's constant and $c$ is the speed of light. The laser intensity was Gaussian in time with an 8 ns FWHM, resulting in a photon flux, $\phi$:

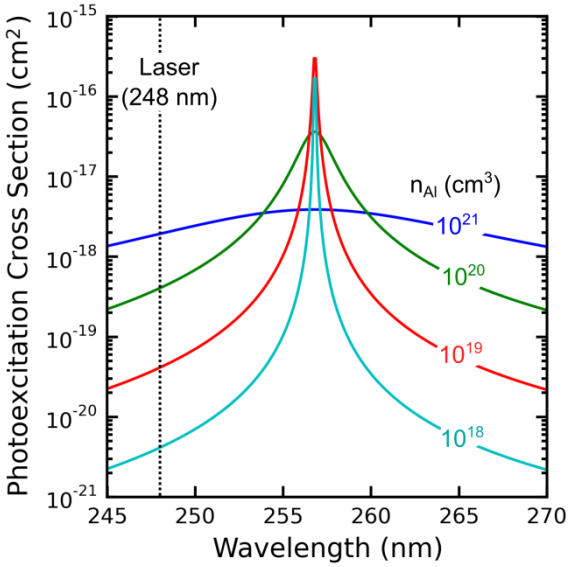


Figure 2. The cross section for photoexcitation of Al to Al($y^2D$) as a function of photon wavelength. The laser wavelength is indicated with the dashed vertical line.

$$\phi = (2.4 \times 10^{26} cm^{-2}s^{-1}) \exp\left(-\frac{t^2}{2.3 \times 10^{-17} s^2}\right). \#(10)$$

The energy equation for gas species is

$$\frac{d\left(\frac{3}{2}k_B N T_g\right)}{dt} = \sum_j^{rxns} \Delta\epsilon_{g,j} R_j - \gamma \frac{\left(\frac{3}{2}k_B N T_g\right)}{V}\frac{dV}{dt}. \#(11)$$

$N$ is the total number density of all heavy species. $\frac{dV}{dt}$ as a function of time is based on an estimate of expansion dynamics to be described in Sec. B.2. The final terms in Eqs. 7 and 10 represent the loss of thermal energy due to isentropic expansion. Though no work is being done in this expansion, the thermal energy is being converted to directed flow of the gas. We consider this conversion of thermal energy to flow as work because it can no longer contribute to the collisionality of the gas.

**B.1. Reaction Mechanism**

The reaction mechanism used in the global model is presented in Table 1. Six electronic excited states are included in this mechanism. Terms with multiple levels due to spin-orbit coupling are grouped into a single species. In calculating cross sections, the transition between levels having the largest cross section is assumed to dominate (when there are multiple levels this will be the allowed transition). The electron impact ionization cross section originates from experimental data, but the electron impact excitation cross sections are estimated using general formulae [23]. Each superelastic collision cross section is calculated from the corresponding excitation cross section by detailed balance [24].

Radiative relaxation is included for states that emit, except for those that have resonant reabsorption by the ground state. By removing radiation reactions which emit to the ground state (e.g. Al($4^2S$) → Al) we are assuming that radiation is reabsorbed and that the plasma is optically thick. It is expected that this is accurate early in time as the density of Al is high and becomes less accurate as the plasma expands.

Direct photoexcitation is included for excitation of the ground state to Al($y^2D$). While the laser wavelength is certainly not on resonance with this transition – 257 nm transition compared to a 248 nm laser – significant pressure broadening can cause the absorption cross section to be significant. The pressure-broadened photoexcitation cross section is shown in Fig. 2. As the density of Al increases from

$10^{18}$ to $10^{21}$ $cm^{-3}$, the cross section at the laser wavelength increases from $4 \times 10^{-21}$ to $2 \times 10^{-18}$ $cm^2$. This pressure broadening (resonance broadening) was calculated by Eq. 15 from Ref. [25], and Doppler broadening is negligible in comparison. In this model, as the Al density increases above $10^{21}$ $cm^{-3}$, the cross section broadens so much that its value at 248 nm begins to decrease. In reality, as the density approaches that of solid Al ($6 \times 10^{22}$ $cm^{-3}$), the Al begins to behave more like a solid, with electron energy levels that differ from that of the Al atoms. Those effects would likely significantly impact the earliest timescales, but, for simplicity, we have neglected them here. The effects of broadening in SPAMS have been observed experimentally using tunable lasers [20].

For each reaction, a change in electron energy ($\Delta\varepsilon_{electron}$) and gas energy ($\Delta\varepsilon_{gas}$) is required, which is used in Eqs. 7 and 11. This approach accounts for the effect of each reaction on electron and neutral energy balance, depending on the type of reaction. For example, when an electron excites Al($3^2$D) to Al($4^2$P), 0.064 eV of energy is lost from the electrons ($\Delta\varepsilon_{electron}$ = -0.064 eV). If this Al($4^2$P) then emits a photon ($\Delta\varepsilon_{electron} = \Delta\varepsilon_{gas} = 0$ eV), that energy which was stored in the excited state is lost from the system as radiation.

**Table 1. Reaction Mechanism Used in the Global Model**

| Reaction | Rate Coefficient[a] | $\Delta\varepsilon_{electron}$ (eV) | $\Delta\varepsilon_{gas}$ (eV) | Reference |
|---|---|---|---|---|
| *Electron impact excitation* | | | | |
| $e^- + Al \rightarrow Al(4^2S) + e^-$ | σ | -3.143 | 0 | [23] |
| $e^- + Al \rightarrow Al(3^4P) + e^-$ | σ | -3.598 | 0 | [23] |
| $e^- + Al \rightarrow Al(3^2D) + e^-$ | σ | -4.021 | 0 | [23] |
| $e^- + Al \rightarrow Al(4^2P) + e^-$ | σ | -4.085 | 0 | [23] |
| $e^- + Al \rightarrow Al(5^2S) + e^-$ | σ | -4.673 | 0 | [23] |
| $e^- + Al \rightarrow Al(y^2D) + e^-$ | σ | -4.827 | 0 | [23] |
| $e^- + Al(4^2S) \rightarrow Al(3^2D) + e^-$ | σ | -0.878 | 0 | [23] |
| $e^- + Al(4^2S) \rightarrow Al(4^2P) + e^-$ | σ | -0.942 | 0 | [23] |
| $e^- + Al(4^2S) \rightarrow Al(5^2S) + e^-$ | σ | -1.53 | 0 | [23] |
| $e^- + Al(4^2S) \rightarrow Al(y^2D) + e^-$ | σ | -1.684 | 0 | [23] |
| $e^- + Al(3^2D) \rightarrow Al(4^2P) + e^-$ | σ | -0.064 | 0 | [23] |
| $e^- + Al(3^2D) \rightarrow Al(5^2S) + e^-$ | σ | -0.652 | 0 | [23] |
| $e^- + Al(3^2D) \rightarrow Al(y^2D) + e^-$ | σ | -0.806 | 0 | [23] |
| $e^- + Al(4^2P) \rightarrow Al(5^2S) + e^-$ | σ | -0.588 | 0 | [23] |
| $e^- + Al(4^2P) \rightarrow Al(y^2D) + e^-$ | σ | -0.742 | 0 | [23] |
| $e^- + Al(5^2S) \rightarrow Al(y^2D) + e^-$ | σ | -0.154 | 0 | [23] |
| *Superelastic* | | | | |
| $e^- + Al(4^2S) \rightarrow Al + e^-$ | σ | 3.143 | 0 | [b] |
| $e^- + Al(3^4P) \rightarrow Al + e^-$ | σ | 3.598 | 0 | [b] |
| $e^- + Al(3^2D) \rightarrow Al + e^-$ | σ | 4.021 | 0 | [b] |
| $e^- + Al(4^2P) \rightarrow Al + e^-$ | σ | 4.085 | 0 | [b] |
| $e^- + Al(5^2S) \rightarrow Al + e^-$ | σ | 4.673 | 0 | [b] |
| $e^- + Al(y^2D) \rightarrow Al + e^-$ | σ | 4.827 | 0 | [b] |
| $e^- + Al(3^2D) \rightarrow Al(4^2S) + e^-$ | σ | 0.878 | 0 | [b] |
| $e^- + Al(4^2P) \rightarrow Al(4^2S) + e^-$ | σ | 0.942 | 0 | [b] |
| $e^- + Al(5^2S) \rightarrow Al(4^2S) + e^-$ | σ | 1.53 | 0 | [b] |
| $e^- + Al(y^2D) \rightarrow Al(4^2S) + e^-$ | σ | 1.684 | 0 | [b] |
| $e^- + Al(4^2P) \rightarrow Al(3^2D) + e^-$ | σ | 0.064 | 0 | [b] |
| $e^- + Al(5^2S) \rightarrow Al(3^2D) + e^-$ | σ | 0.652 | 0 | [b] |

| | | | | |
|---|---|---|---|---|
| $e^- + Al(y^2D) \rightarrow Al(3^2D) + e^-$ | σ | 0.806 | 0 | [b] |
| $e^- + Al(5^2S) \rightarrow Al(4^2P) + e^-$ | σ | 0.588 | 0 | [b] |
| $e^- + Al(y^2D) \rightarrow Al(4^2P) + e^-$ | σ | 0.742 | 0 | [b] |
| $e^- + Al(y^2D) \rightarrow Al(5^2S) + e^-$ | σ | 0.154 | 0 | [b] |
| *Electron impact ionization* | | | | |
| $e^- + Al \rightarrow Al^+ + e^- + e^-$ | σ | -5.985 | 0 | [26] |
| $e^- + Al(4^2S) \rightarrow Al^+ + e^- + e^-$ | σ | -2.842 | 0 | [23] |
| $e^- + Al(3^4P) \rightarrow Al^+ + e^- + e^-$ | σ | -2.388 | 0 | [23] |
| $e^- + Al(3^2D) \rightarrow Al^+ + e^- + e^-$ | σ | -1.976 | 0 | [23] |
| $e^- + Al(4^2P) \rightarrow Al^+ + e^- + e^-$ | σ | -1.901 | 0 | [23] |
| $e^- + Al(5^2S) \rightarrow Al^+ + e^- + e^-$ | σ | -1.313 | 0 | [23] |
| $e^- + Al(y^2D) \rightarrow Al^+ + e^- + e^-$ | σ | -1.171 | 0 | [23] |
| *Elastic* | | | | |
| $e^- + Al \rightarrow e^- + Al$ | σ | elastic | elastic | [27] |
| $e^- + Al^* \rightarrow e^- + Al^*$ | σ | elastic | elastic | [c,d] |
| $e^- + Al^+ \rightarrow e^- + Al^+$ | σ | elastic | elastic | [24] |
| *Penning ionization* | | | | |
| $Al^* + Al^* \rightarrow Al + Al^+ + e^-$ | $1.89\times10^{-10}T_g^{0.5}$ | [e] | 0 | [28][c] |
| *Recombination* | | | | |
| $e^- + Al^+ \rightarrow Al$ | $k_{RR}$[f] | 0 | 0 | [29] |
| $e^- + Al^+ \rightarrow Al$ | $k_{DR}$[g] | 0 | 0 | [30] |
| $e^- + Al^+ + e^- \rightarrow Al + e^-$ | $k_{TBR}$ | 0 | 0 | [31] |
| *Quenching* | | | | |
| $Al^* + Al \rightarrow Al + Al$ | $5\times10^{-10}T_g^{0.5}$ | 0 | [h] | [32][c,i] |
| *Radiation* | | | | |
| $Al(4^2P) \rightarrow Al(3^2D)$ | $7.10\times10^{2}$ s$^{-1}$ | 0 | 0 | [33] |
| $Al(5^2S) \rightarrow Al(4^2P)$ | $6.00\times10^{6}$ s$^{-1}$ | 0 | 0 | [33] |
| $Al(y^2D) \rightarrow Al(4^2P)$ | $9.89\times10^{6}$ s$^{-1}$ | 0 | 0 | [33] |
| *Photon reactions* | | | | |
| $h\nu + h\nu + Al \rightarrow Al^+ + e^-$ | $8.27\times10^{-48}$ cm$^4$s | 4.015 | 0 | [15] |
| $h\nu + e^- + Al \rightarrow e^- + Al$ | $1.76\times10^{-38}T_e^{-0.5}$ cm$^5$ | 5.00 | 0 | [15][j] |
| $h\nu + e^- + Al^+ \rightarrow e^- + Al^+$ | $2.51\times10^{-37}T_e^{-0.5}$ cm$^5$ | 5.00 | 0 | [15][j] |
| $h\nu + Al(4^2S) \rightarrow Al^+ + e^-$ | $3.15\times10^{-18}$ cm$^2$ | 2.158 | 0 | [34, 35] |
| $h\nu + Al(3^4P) \rightarrow Al^+ + e^-$ | $2.04\times10^{-18}$ cm$^2$ | 2.613 | 0 | [34, 35] |
| $h\nu + Al(3^2D) \rightarrow Al^+ + e^-$ | $1.25\times10^{-18}$ cm$^2$ | 3.036 | 0 | [34, 35] |
| $h\nu + Al(4^2P) \rightarrow Al^+ + e^-$ | $1.16\times10^{-18}$ cm$^2$ | 3.099 | 0 | [34, 35] |
| $h\nu + Al(5^2S) \rightarrow Al^+ + e^-$ | $4.58\times10^{-19}$ cm$^2$ | 3.688 | 0 | [34, 35] |
| $h\nu + Al(y^2D) \rightarrow Al^+ + e^-$ | $3.35\times10^{-19}$ cm$^2$ | 3.842 | 0 | [34, 35] |
| $h\nu + Al \rightarrow Al(y^2D)$ | σ(Al) | 0 | 0 | [k] |

(a) $T_e$ and $T_g$ are in K. Rates are in units of cm$^3$/s for 2-body reactions and cm$^6$/s for 3-body reactions except where indicated otherwise.

(b) Cross sections for superelastic collisions are obtained by detailed balance of the excitation cross sections.
(c) Al* refers to Al($4^2$S), Al($3^4$P), Al($3^2$D), Al($4^2$P), Al($5^2$S), and Al($y^2$D)
(d) Cross section for elastic collisions with excited states is assumed to be the same as elastic collisions with the ground state.
(e) For each combination of excited states, the change in electron energy is determined by adding the excitation energy of the excited states and subtracting the ionization potential. This ranges from 0.3-3.7 eV.
(f) Radiative recombination.
(g) Dielectronic recombination.
(h) The gas heating as a result of collisional quenching is assumed to be the excitation energy of the excited state.
(i) Rate estimated to be on the order of that of $N_2$* quenching.
(j) This rate for inverse Bremsstrahlung ignores stimulated emission.
(k) Based on pressure broadening of transition to state at Al($y^2$D), see Fig. 2.

**B.2. Expansion into Vacuum**

The expansion speed of the gas into the surrounding vacuum is assumed to take the form

$$v(t) = v_\infty\left(1 - \exp\left(-\frac{t}{\tau}\right)\right) \#(12)$$

$$v_\infty = \sqrt{\frac{3k_B T_0}{m_{Al}}} \#(13)$$

where $v(t)$ is the speed of the expansion at time $t$, $v_\infty$ is the expansion speed at infinite time, and $\tau$ is the characteristic timescale of the expansion, which is assumed to be 10 ns except where indicated. The value of $v_\infty$ is approximated by assuming that all the initial thermal energy ($3k_BT_0/2$) is converted to kinetic energy ($m_{Al}v_\infty^2/2$). $T_0$ is the initial temperature, which is assumed to be 2,000 K, and $m_{Al}$ is the atomic mass of Al. (The value of $T_0$ had a very minor impact on the results.) This approach does not account for additional energy deposited in the plasma after vaporization (e.g., inverse Bremsstrahlung heats electrons, elastic collisions then heat the background gas) or any losses of thermal energy due to the generation of excited states or ions.

Eq. 12 is a highly simplified approach, which is a functional form that was selected because it captures the expected qualitative behavior without causing negative (unphysical) temperatures at long timescales. Eq. 12 is used to calculate the values of $V$ and $dV/dt$ used in Eqs. 1, 5-7, and 11 by assuming a spherical plume. By using Eq. 12, the phase change is approximated as a particle that is instantaneously and uniformly vaporized at $t_0$, and then allowed to expand. The lack of available data on the expansion dynamics in these particular conditions is a primary source of uncertainty in this model, and an important topic for future work. The expansion is consistent with the order of magnitude observed by Cabalo where in a SPAMS system with two laser pulses, expansion to ~$10^{-3}$ m occurs in ~$10^{-6}$ s after the first laser pulse [36]. The selected value of $v_\infty$ would be expected to cause a variation in the collection time of at least $10^{-9}$-$10^{-8}$ s which is consistent with experimental observations (though there are other processes which also contribute to broadening of time-of-flight peaks in spectra). However, even the order of magnitude of the timescale, $\tau$, is not well known, and therefore the sensitivity of the results to this parameter is discussed in Sec. III, Part E. The assumed expansion dynamics are shown in Fig. 3. Ion-ion repulsion is not included because the plasma is quasineutral.

**B.3. Initial Conditions and Numerical Parameters**

We assume that the system transitions to a state describable by a global model (i.e., a gas) at the peak laser intensity, which corresponds to $t$ = 0 s. In reality, this transition is continuous and will vary depending on location within the particle, particle size, and laser intensity. The initial conditions for the

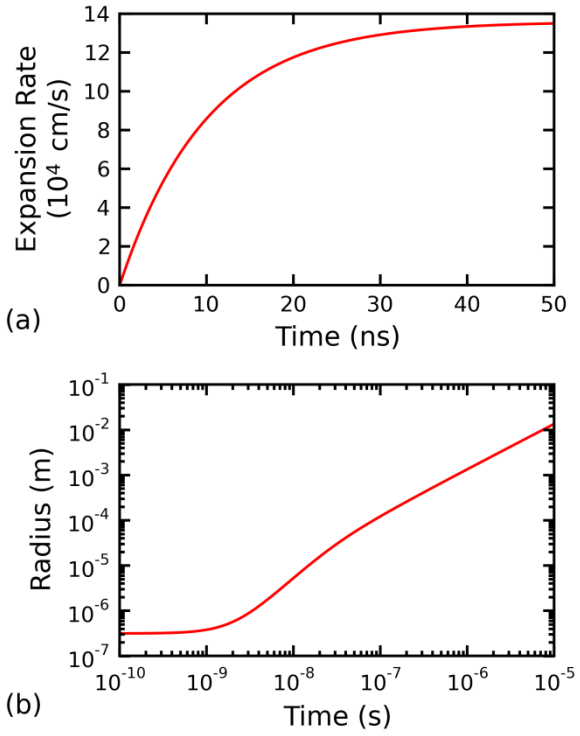


Figure 3. The assumed expansion dynamics of the vaporized Al volume. $t = 0$ s corresponds to the time of the maximum laser intensity. (a) The speed assumed by Eq. 12 for an expansion timescale, τ, of 10 ns. The expansion rate exponentially approaches the speed at which all thermal energy has been converted into kinetic energy of the expansion (Eq. 13). (b) The radius as a function of time in the base case assuming the expansion rate in Eq. 12.

plasma simulation are $T_e = T_g = 2{,}000$ K with a total density of heavy species that is equivalent to the density of solid aluminum. Ground state Al and its excited states are Boltzmann distributed according to the gas temperature.

The initial electron and ion densities are set to be the minimum of $10^{11}$ cm$^{-3}$ and $1/V_0$, where $V_0$ is the initial volume, and the electron density that would occur thermally. In the base case this is limited by $1/V_0$ (i.e., one electron in the initial volume), which is $n_e = n_i = 7 \times 10^{12}$ cm$^{-3}$. This is equivalent to an ionization fraction of $1 \times 10^{-10}$. In the base case, the total initial excitation fraction is $6 \times 10^{-9}$.

In these conditions, it is unlikely that the laser will vaporize the entire particle. The initial volume in the global model was determined by the amount of material that would be vaporized during the first half of the laser pulse (before the laser reaches its maximum intensity at $t = 0$ s), which was calculated as follows. The energy required to vaporize Al was determined from the integral of the temperature dependent specific heat [37], and the heats of vaporization [38] and fusion [39]. The amount of energy required to vaporize room temperature Al is $1.2 \times 10^4$ J/g. The energy deposited in the particle by the laser was calculated by

$$E_{dep} = (1 - \rho_{248})\pi r_{particle}^2 \varepsilon_{photon} \int_{-\infty}^{0} \phi(t) dt \quad \#(14)$$

where $\rho_{248}$ is the reflectance of the particle at 248 nm, $r_{particle}$ is the solid particle radius, $\varepsilon_{photon}$ is the laser photon energy (4.999 eV) and $\phi$ is the laser photon flux. In reality, the vaporization is likely to occur as a vaporization front, in which the laser deposits its energy in a layer several nm thick [40, 41]. At room temperature the reflectivity of aluminum is 92% for 248 nm [40], but above the melting temperature, there are less data available and estimates range from 20-90% [42]. A reflectance of 60% was used in this work

[43]. Based on Eq. 14, the laser energy deposited by the start time for the global model (the first half of the laser pulse) is 4 nJ. Based on the $1.2 \times 10^4$ J/g required for vaporization, this energy can vaporize approximately $1.3 \times 10^{-13}$ $cm^3$ of Al. A few aspects of the model require an area (e.g., diffusion losses and the maximum number of photons which may be absorbed). Although the cloud of Al vapor is not likely to be spherical throughout the expansion, for simplicity it is approximated as spherical where an area is required. The initial radius of the plume based on the spherical assumption is 310 nm.

The system of equations described in Eqs. 1-10 were integrated using the odeint library in Python. odeint uses adaptive internal timesteps and implicit methods when the problem becomes stiff. The timesteps at which the solution was requested from odeint were distributed logarithmically beginning with a timestep of $10^{-17}$ s and increasing to $6 \times 10^{-9}$ by the end of the simulation at $10^{-5}$ s. A typical runtime on a single processor is 30 minutes.

## III. Modeling Ionization of an Al Particle

In this section, the results for the base case, which is a 1 μm particle and an 8 mJ laser pulse, are discussed in detail in Parts A and B. Then the effect of varying the laser intensity is discussed in Part C, the effect of particle diameter is discussed in Part D, and the effect of the characteristic timescale of expansion is discussed in Part E.

### A. Non-equilibrium Plasma Chemistry

The density and number of atoms, ions, and electrons of each of the species are shown over time in Fig. 4. The density of Al begins at the solid density of $6 \times 10^{22}$ $cm^{-3}$ and decreases rapidly as the particle expands, reaching $8 \times 10^{11}$ $cm^{-3}$ by 1 μs. The number of atoms, ions, and electrons (the number density multiplied by the plasma volume) is plotted in Fig. 4b to better illustrate how the excitation and ionization fraction vary in time. By the end of the simulation the plasma has expanded to several cm in diameter. The gas temperature, electron temperature, and the photon flux are shown in Fig. 5 with an inset showing the low temperatures that occur at longer timescales.

The Al($y^2D$) state is initially the most abundant excited state because it can be excited directly by the laser from the ground state. Al($y^2D$) is also the excited state with the largest excitation energy included in the model. As the electron density increases in the first few ns, superelastic collisions between electrons and Al($y^2D$) begin to populate lower excited states. These superelastic collisions also increase the electron temperature ($T_e$), which then enables a variety of other reactions, including electron impact excitation of the ground state and ionization of excited states. In general, the increased electron density allows for more transfer of energy between different excitation/ionization states. This leads to an increase in the number of atoms in each of the other excited states between 1 and 4.5 ns. Despite this, at this laser intensity, the ground state is not significantly depleted, and the excitation fraction does not exceed 0.7% for all species. At 4.2 ns, the electron temperature reaches a local maximum of 7,100 K (0.6 eV) and then decreases rapidly to 5,300 K (0.5 eV) by 10 ns. (Higher electron temperatures briefly occur in the early timescales of the simulation, but few electrons are present at the time, so the impact on excitation and ionization is negligible). As the laser intensity decreases significantly, and the pressure broadening becomes less significant, the Al($y^2D$) state is not repopulated as rapidly. After 4.5 ns, the number of excited state atoms decreases due to radiation (for Al($5^2S$) and Al($y^2D$)) and collisional quenching (for all excited states). By approximately 40 ns, the excited state densities cease to change significantly. This occurs because the expansion into vacuum has caused the densities and temperatures to decrease, so the collision frequency decreases, and the quenching rate ceases to be significant.

For the first 6 ns, Al($3^4P$) is the least abundant excited state. Because this state involves exciting an electron from a different orbital than any of the other states, it is not populated by superelastic collisions from higher excited states; it is only generated by inelastic collisions of electrons with the ground state.

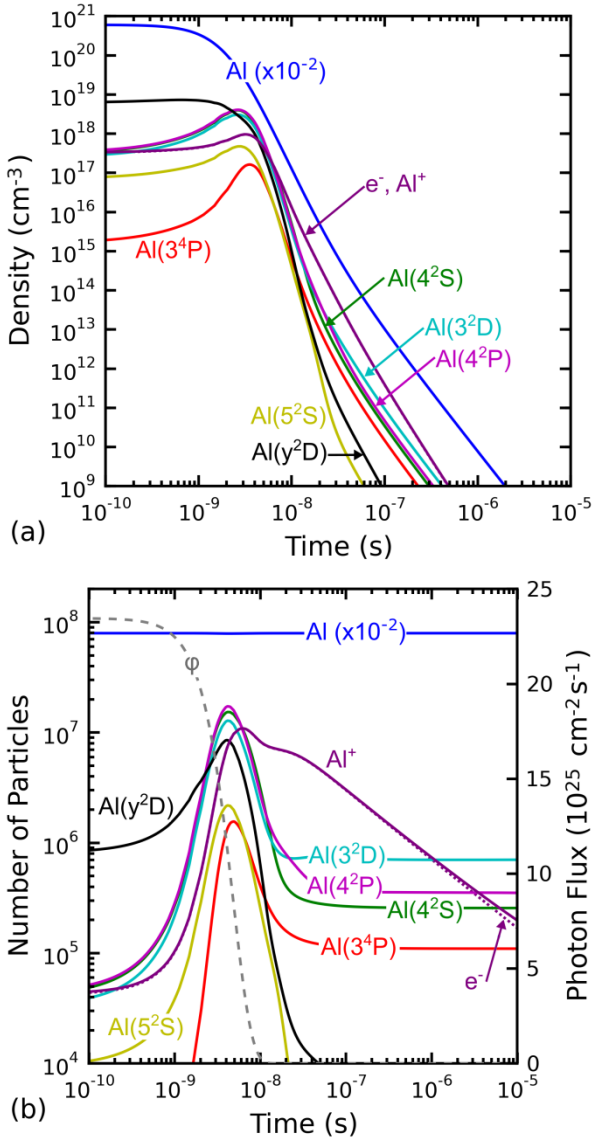


Figure 4. (a) The density of each species as a function of time in the base case. (b) The number of particles (electrons, ions, and atoms) plotted over the same time period (the density times the plasma volume). The electron density is indicated with a dashed line. It deviates from the ion density by 15% by $10^{-5}$ s. The photon flux ($\phi$) is Gaussian in time with an 8 ns FWHM. $t = 0$ is defined as the maximum laser intensity.

The electron temperature ($T_e$) and the gas temperature ($T_g$) both continue to decrease until the end of the simulation due to the isentropic expansion. The inset in Fig. 5 shows $T_e$ as low as 0.2 K and $T_g$ as low as $10^{-3}$ K. In reality, more complex behavior would likely dominate in the vacuum limit. Ultracold plasmas are known to have an additional electron heating mechanisms (disorder-induced heating) that, for simplicity, is not included here. When the neutral collision frequency decreases sufficiently, the gas temperature ceases to be isotropic and may not continue to decrease [44, 45].

The number of ions reaches a maximum of $1 \times 10^7$ (ionization fraction of 0.1%) at 6 ns and then slowly decreases due to the recombination rate exceeding the ionization rate. The details of the ionization mechanisms will be discussed in Part B. The difference in the number of electrons and ions is negligible for the majority of the simulation, although the number of electrons is 15% lower than the number of ions

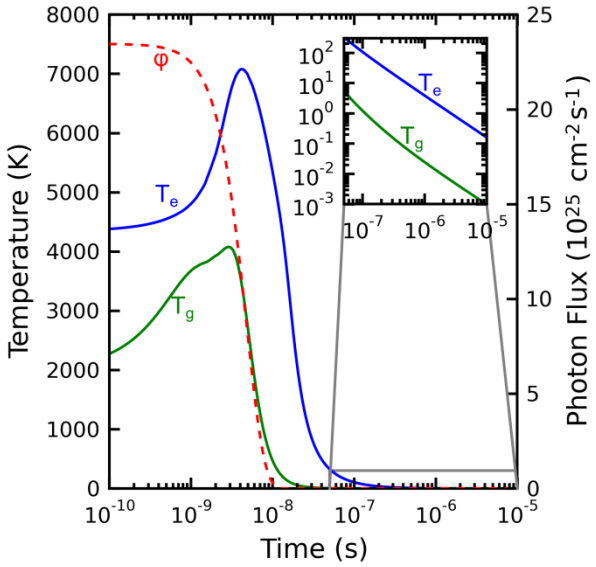


Figure 5. The electron temperature ($T_e$) and gas temperature ($T_g$) as a function of time in the base case. The photon flux ($\phi$) is Gaussian in time with an 8 ns FWHM and is shown for reference.

at the end of the simulation. This difference occurs because electrons are allowed to diffuse out of the plasma volume (see Eq. 4). The diffusion of electrons is a relatively small effect because the positive charge is sufficient to retain most of the electrons.

Though experimental measurements of the electron density in these exact conditions are not available, in similar conditions in a Cu plasma produced by 1064 nm laser ablation of a flat target, electron densities of $6 \times 10^{17}$ cm$^{-3}$ were observed via Stark broadening [46]. This density is very similar to the maximum electron density of $9 \times 10^{17}$ cm$^{-3}$ calculated in this case, although the conditions and the likely ionization mechanisms are quite different.

In order to better understand how the laser energy is coupled to the particle, the primary reactions that result in the absorption of the 248 nm photons are plotted in Fig. 6. The reaction rates (with units of cm$^{-3}$s$^{-1}$) are multiplied by the plasma volume to determine the total number of photons absorbed per second. This quantity will be referred to as the global rate. Throughout the simulation, the primary mechanism of photon absorption from the laser is direct photoexcitation at a highly pressure-broadened transition:

$$h\nu + Al \rightarrow Al(y^2D). \quad (15)$$

The cross section of this absorption at 248 nm has a maximum at an Al density of $1 \times 10^{21}$ cm$^{-3}$ (2% of the density of solid Al). Above this density, the pressure broadening assumption used in the calculation of the cross section may cease to be accurate as molecular orbitals become relevant. During the first 4 ns of the simulation, even though the laser energy is decreasing, the number of photons absorbed increases. The decreasing density of Al in this initial expansion leads to a larger photoabsorption cross section for photoexcitation. The photoabsorption cross section reaches a maximum at an Al density of $1 \times 10^{21}$ cm$^{-3}$, which occurs at 4 ns in this simulation. As the particle plume expands further, the Al density decreases, the pressure broadening decreases, and the direct photoexcitation cross section decreases.

All other photon absorption processes have a global rate that is at least an order of magnitude lower than that of direct photoexcitation. Two-photon ionization is more common early in time but decreases quickly because its global rate scales with $\phi^2$, where $\phi$ is the photon flux. The fact that two-photon ionization is monotonically decreasing is a result of selecting the start of the global model at the maximum laser intensity. As the excitation fraction increases, photoionzation of excited states ($h\nu + Al^* \rightarrow Al^+ + e^-$) becomes significant. The global rate of inverse Bremsstrahlung with neutrals ($h\nu + e^- + Al \rightarrow Al + e^-$) is several orders of magnitude below the other processes. This differs from previous models of LIBS plasmas in which this mechanism was a dominant heating mechanism, and this difference is in part due to the shorter

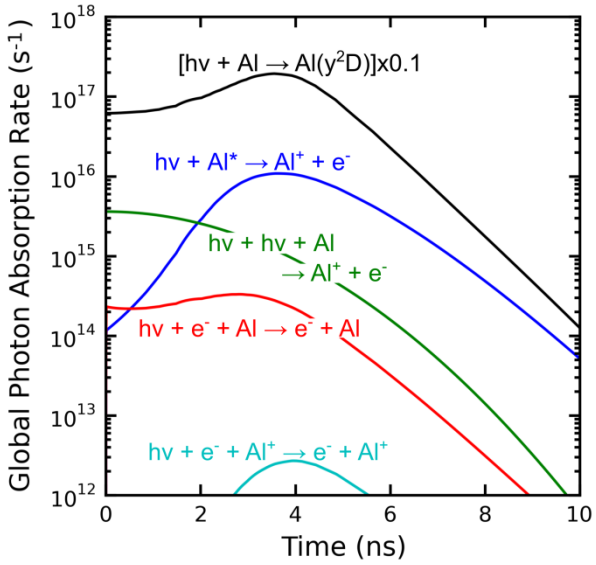


Figure 6. The primary photoabsorption mechanisms in the base case. The global rate refers to the volumetric rate ($R_j$) multiplied by the plasma volume ($V$). Al* refers to the sum over all excited states.

wavelength used here [15, 16]. The contribution of inverse Bremsstrahlung with ions is essentially negligible here compared to the other photon absorption processes. The importance of pressure-broadened photoexcitation described here has been observed experimentally; when slightly varying the laser wavelength in a SPAMS device near resonant absorption lines for several metals, the number of metal ions in the spectra changed significantly [20].

**B. Ionization and Recombination Mechanisms**

A critical question for understanding and improving SPAMS devices is: How are the ions produced? A related question is: How many ions survive to be collected? The first question can be answered by a discussion of the data in Fig. 7. The ionization rates ($cm^{-3}s^{-1}$) have been multiplied by the plasma volume in order to calculate the number of ions which are produced per second. The main sources of ionization, grouped into categories, are shown in Fig. 7a on a log-scale. More detail on the specific reactions that are most important are shown in Fig. 7b.

The dominant reaction for the production of ions (by 2 orders of magnitude) is electron impact ionization of excited states, $e^- + Al^* \rightarrow Al^+ + e^- + e^-$. The global rate of this interaction reaches a maximum at 4 ns. This maximum is slightly earlier than the maximum $T_e$ and the maximum number of excited Al atoms, because this global reaction rate increases with density. Electron impact ionization of Al(y$^2$D) is the dominant ion-producing reaction in this simulation. Although it is not the most abundant excited state at 4 ns, it has the lowest threshold energy for ionization (1.171 eV). The ionization frequencies of other excited states are lower by at least a factor of 4. Because these reactions require at least 1.171 eV of electron energy (the threshold to ionize Al(y$^2$D)), they are highly sensitive to $T_e$. The total global reaction rate decreases from $1 \times 10^{18}$ $s^{-1}$ to $7 \times 10^{14}$ $s^{-1}$ from 4 to 10 ns. In this period the densities have decreased by 2 orders of magnitude due to expansion, which would account for a reduction in the global reaction rate by the same factor. The excited state populations decrease due to quenching and radiation, which accounts for an additional order of magnitude decrease in global rate. $T_e$ decreases from 7,100 K (0.6 eV) to 5,300 K (0.5 eV), which accounts for approximately an additional factor of 2 decrease in the global rate.

Electron impact ionization of the ground state has a much higher threshold energy (5.985 eV), and therefore has a much lower rate, despite the ground state having a density several orders of magnitude higher than the excited states. Two-photon ionization is the dominant ionization mechanism at the shortest timescales ($10^{-12}$ s), before the excited state densities have become significant, but overall does not produce

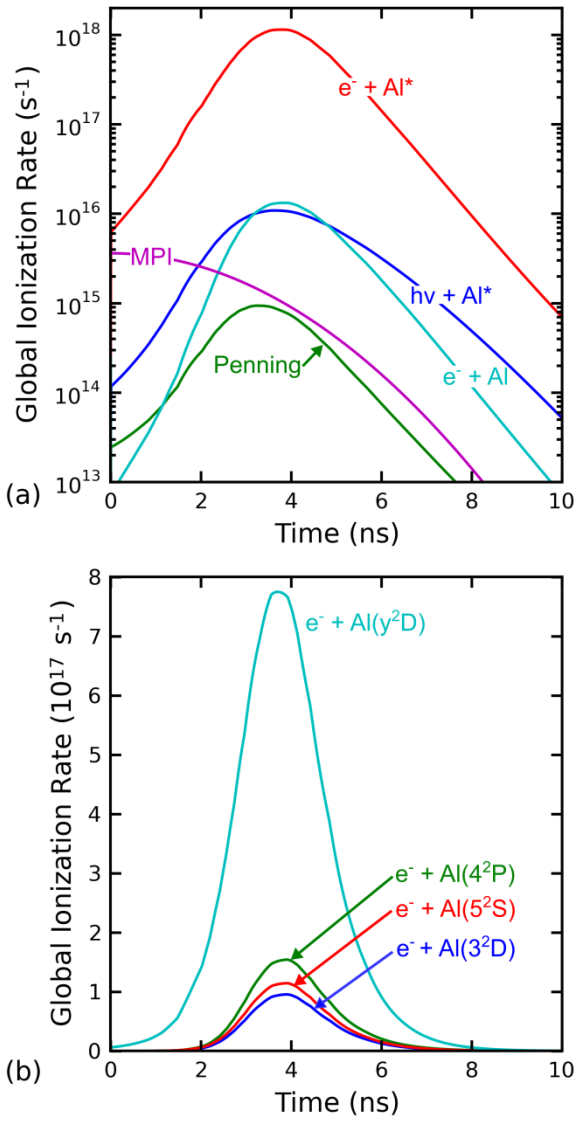


Figure 7. Ionization mechanisms of a 1 μm Al particle with an 8 mJ laser. (a) The main sources of ionization, grouped into categories. Al* refers to all excited states of Al included in the model. "MPI" refers to multiphoton ionization, which in this case is limited to two-photon ionization. (b) The primary sources of ions, for the four most significant ionization reactions, with each reaction labeled by its reactants. Note that the y-axis is on a logarithmic scale in (a) and a linear scale and in (b).

a significant fraction of the ions. All of the excited states have enough energy that they can be directly ionized by the laser, and this process produces a number of ions that is comparable to electron impact ionization of the ground state. Penning ionization ($Al^* + Al^* \rightarrow Al^+ + e^- + e^-$) is the least significant process considered here.

In this model, the electron energy distribution function is assumed to be Maxwellian, but this can be violated in low temperature plasmas. Often, the distribution function is depleted above the threshold for inelastic processes (in this case 3.143 eV for excitation of Al). However, because electron impact ionization and excitation of the ground state (rates which would be most sensitive to these non-Maxwellian effects) provide relatively minor contributions to the production of ions and excited states, this deviation is less likely to critically impact the results discussed here.

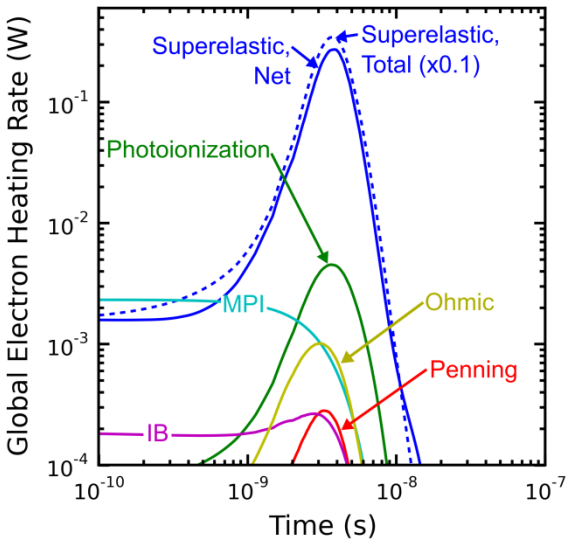


Figure 8. The rate of electron heating in the base case by different processes as a function of time. This includes superelastic collisions ("Superelastic"), photoionization, multiphoton ionization ("MPI"), Ohmic heating, Penning ionization, and inverse Bremsstrahlung radiation ("IB"). Superelastic collisions are plotted as total (reduced by a factor of 10) and the net heating. The net superelastic collisions is the superelastic heating minus that of the reverse reactions (electron energy losses due to excitation).

Because electron impact of excited states are the most important ionization processes, and because they are sensitive to $T_e$, the causes of electron heating processes are also important to understand. The most significant heating processes are plotted in Fig. 8. The heating rate due to (net) superelastic collisions is two orders of magnitude larger than any other heating rate. The net superelastic heating rate subtracts the electron energy losses due to the reverse reactions (electron impact excitation). At equilibrium the forward and reverse rates would balance, and the net superelastic heating rate would be zero. In photoionization reactions where the photon energy is in excess of the energy required for ionization (photoionization of excited states and multiphoton ionization), the electrons receive that excess energy. These processes are the next most significant for electron heating.

The second important question in this system is: How many ions survive?. Based on Fig. 4b, the number of ions decreases by almost 2 orders of magnitude from its maximum value over 10 μs. The recombination rate of ions in comparison to the global ionization rate is shown in Fig. 9. Three-body recombination results in 5 orders of magnitude more recombination reactions than two-body (dielectronic or radiative) recombination. The three-body reaction rate increases as $T_e$ decreases. Most recombination rates are proportional to $T_e^{-9/2}$, which can result in unphysically large rates at low temperatures. The rate of three-body recombination in the low temperature limit is still not well understood, but we use the method of Hahn to apply some conceptual limits to this rate depending on the plasma density [31]. This method refines the choice of the principal quantum number above which thermal ionization is assumed to occur, which is used in the derivation of three-body recombination rates, based on the plasma density and temperature. The volume integrated recombination rate ($n_e^2 n_{Al+} k_{TBR} V$), reaches a maximum value of $1 \times 10^{18}$ s$^{-1}$ at 3.8 ns. At this point the rate of ionization is only 0.4% larger than that of recombination. The reaction rate increases significantly as $T_e$ approaches 0.2 K at $10^{-5}$ s in this model, but because the plasma is rapidly expanding and the densities are decreasing, the volume integrated recombination rate decreases. Approximately $2 \times 10^9$ ions are produced in the base case, but most are lost to recombination, leaving only $2 \times 10^5$ ions at $10^{-5}$ s. These results are very sensitive to the recombination rate. This model does not include

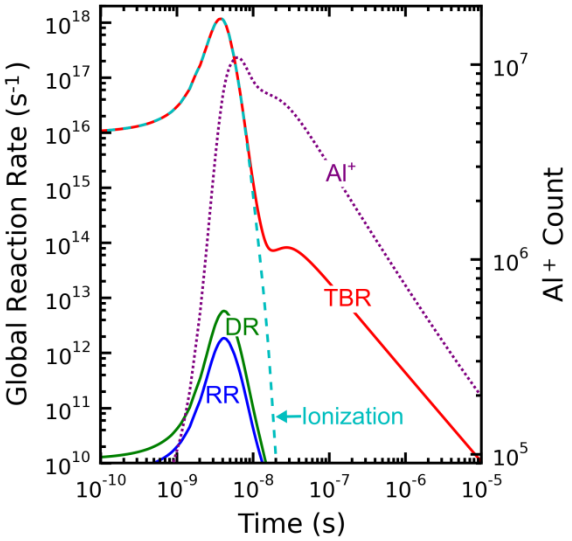


Figure 9. The global reaction rate for each recombination reaction compared with the total ionization rate (dashed) as a function of time. Recombination processes include three-body recombination, $e^- + Al^+ + e^- \rightarrow Al + e^-$ ("TBR"), dielectronic recombination ("DR"), and radiative recombination ("RR"). The total number of $Al^+$ ions (dotted) is plotted on the right axis.

the effects of an externally applied electric field, but this is the subject of future work. We expect that at some timescale (likely μs) the electrons and ions would be separated by this applied field, and recombination would be halted.

**C. Laser Intensity**

To illustrate the effect of the laser power, the intensity of the laser was varied from 6 to 12 mJ for a 1 μm Al particle. The simulation still begins at the maximum laser intensity, but when the laser energy is higher, a greater amount of Al has been ablated. Therefore, the initial plasma volume is larger. Under these assumptions, the number of Al atoms that are vaporized increases from $6 \times 10^9$ for 6 mJ to $1 \times 10^{10}$ for 12 mJ. The initial temperature was held constant at 2,000 K.

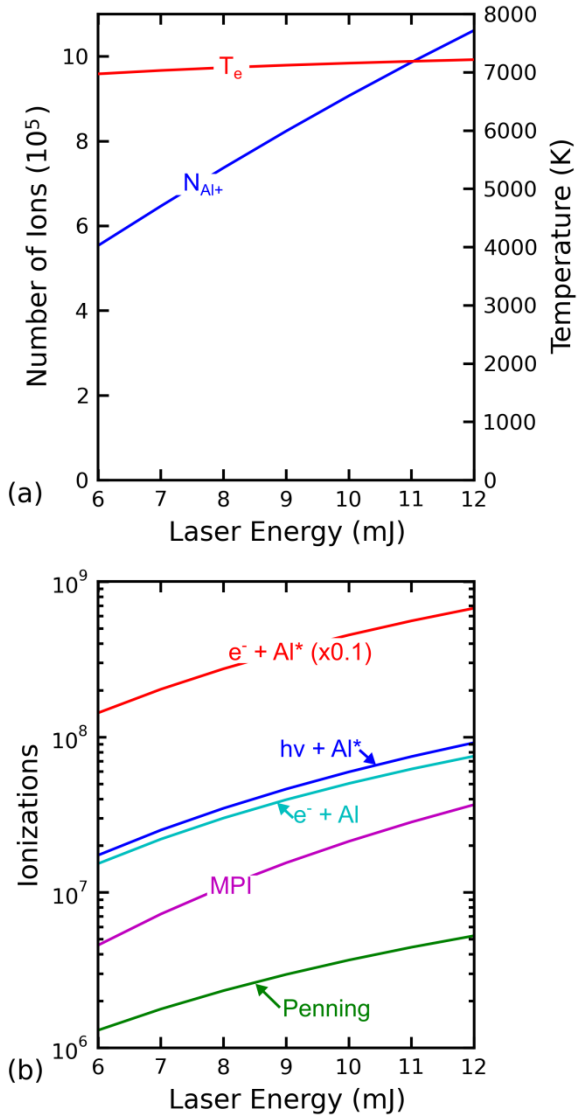


Figure 10. (a) The number of $Al^+$ ions at 1 μs and the maximum value of $T_e$ for $t > 10^{-10}$ s as a function laser energy. (b) The time-integrated, relative contribution of each reaction to the production of $Al^+$.

The total number of ions produced increases approximately linearly with laser energy, as shown in Fig. 10a. The comparison is made at 1 μs, which is the timescale of collection of ions in SPAMS systems. The total number of ions increases by nearly a factor of two from $5.5 \times 10^5$ to $11 \times 10^5$ as the laser energy doubles. This simple proportionality is unexpected. We would expect that doubling the laser energy leads to double the ablated aluminum, but also that due to the higher photon flux, the excitation fraction would be larger and each ablated Al atom would have a higher probability of being ionized, due to increases in the rates of various electron heating and ionization processes. The maximum value of $T_e$ for $t > 10^{-10}$ s is also shown in Fig. 10a. (In each simulation there is a period of even higher $T_e$ at much shorter timescales, $t < 10^{-12}$ s, but it is too brief to produce significant ionization or excitation and is therefore ignored in this analysis.) The maximum value of $T_e$ for $t > 10^{-10}$ s changes negligibly with the laser intensity, which is also unexpected. Although the energy deposited in the plasma increases with laser energy, this energy is

deposited into a larger number of electrons, and the excitation fraction is higher, so the energy lost to electron impact excitation and ionization also increases.

The total number of ionizations, which are the time- and volume-integrated rates, are shown in Fig. 10b. These values scale more as expected. Electron impact ionization of excited states is still the dominant ionization mechanism for all of the laser energies studied here. The number of ionizations by this process increases from $1 \times 10^9$ to $7 \times 10^9$ as the laser energy doubles. This factor of 7 increase is the combined effect of the increase in the total number of atoms (by a factor of 2), the increased excitation fraction (by 25%), and the increased ionization fraction (by 15%) with only a slight increase in temperature. Because the ionization fraction increases, there is a commensurate increase in the three-body recombination rate, which scales as $n_e^2 n_{Al+}$. This increased recombination indicates that a factor of 7 increase in ionizations can still only lead to a factor of 2 increase in the number of ions that survive to μs timescales.

The two-photon ionization rate scales with the laser intensity squared, and therefore increases with a greater slope (on a log scale) than the other reactions. In this range, it still contributes more than two orders of magnitude fewer than other processes.

**D. Particle Diameter**

For a SPAMS system to perform well in a real environment, it must be able to produce ions efficiently across a range of particle sizes. The results for various particle diameters, 400 nm to 8 µm are shown in Fig. 11. The laser intensity was the same for each simulation (8 mJ in a 1 mm by 0.5 mm beam), so particles with a larger cross-sectional area can absorb more light. Therefore, the number of vaporized atoms increased from $1 \times 10^9$ to $5 \times 10^{11}$ as a spherical Al particle increases from 400 nm to 8 µm in physical diameter, as shown in Fig. 11a. Despite a factor of 500 increase in the number of Al atoms vaporized, the number of ions only varies by approximately a factor of 3 over this range of sizes. The maximum value of $T_e$ decreases from 7,200 to 5,600 K with increasing particle diameter.

For smaller diameter particles, the Al vapor cloud is optically thin for the entire simulation. However, for a diameter of 2 µm or more, the plasma absorbs every incident photon. Recall that the rates of reaction that use the photon flux do not account for attenuation (i.e., they assume the flux is uniform),

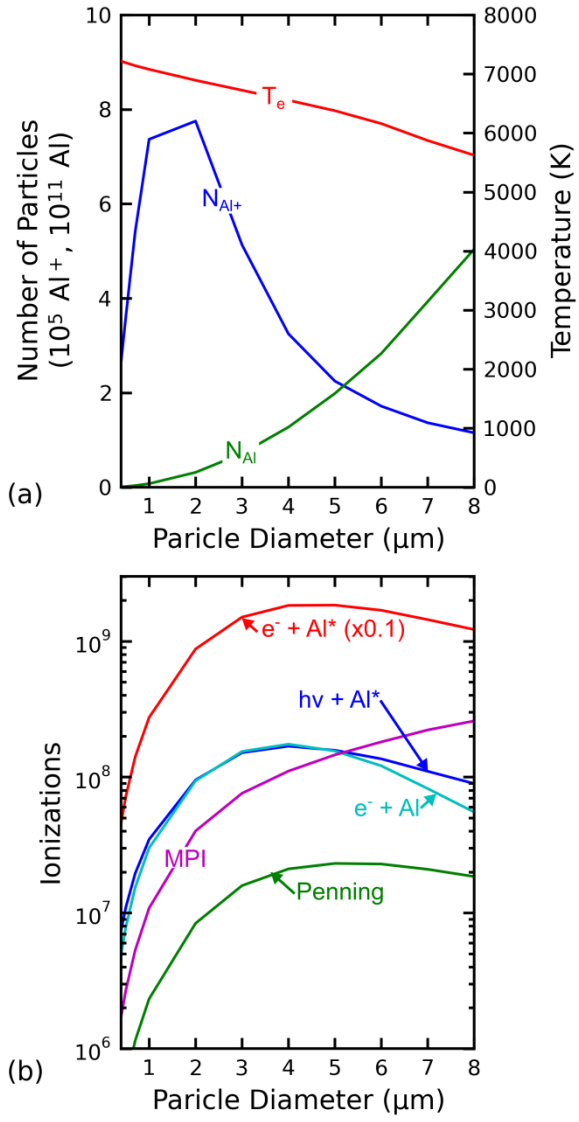


Figure 11. (a) The number of $Al^+$ ions at 1 µs, the total number of vaporized atoms, and the maximum value of $T_e$ for $t > 10^{-10}$ s as a function of particle diameter from 0.4 to 8 µm. (b) The time-integrated, relative contribution of each reaction to the production of $Al^+$ as a function of particle diameter.

but the rates are limited by enforcing the total number of absorbed photons cannot exceed the total number of incident photons. This limit was reached for particles of 2 μm or more. In this volume-averaged simulation, as the particle diameter is increased above 2 μm, roughly the same amount of energy is deposited in a larger volume. This leads to lower temperatures, ionization fractions, and excitation fractions. In the end, this reduces the total number of ions produced for larger particles, however the overall accuracy of the model in this optically-thick limit comes into question.

The primary ionization processes are shown in Fig. 11b. The number of multiphoton ionization events increases as the particle diameter increases from 0.4 to 2 μm as a direct result of the increased number of Al atoms, since the laser intensity is the same in each case. The other ionization mechanisms have more complex dependences on particle diameter. Electron impact ionization of excited states is still the dominant ionization mechanism for all diameters. There is a local maximum in the number of ionizations by this process at 4-5 μm. Above this value, the decreasing $T_e$ and excitation fraction overcome the influence of the larger total plasma volume.

The decrease in the total number of ions produced from 2 to 8 μm is likely overestimated by the volume-averaged approximation used here. As the plasma volume increases to become optically thick, the excitation fraction and ionization fraction would become more nonuniform. The side of the Al vapor cloud on which the laser is incident would have a locally higher $T_e$, excitation fraction, and ionization fraction. This nonuniformity may result in a greater number of total ionizations than we have predicted in this model, though it may be counteracted to some extent by a higher recombination rate.

### E. Expansion Rate

The characteristic time of expansion into vacuum, $\tau$, is unknown in this set of conditions, and an arbitrary value of 10 ns was chosen. This value appears to be reasonable based on comparisons with the expansion rates inferred by experiments of Cabalo *et al*. [36]. To illustrate the impact of this selection, results using multiple values of τ: 1 ns, 10 ns, and 100 ns are shown in Fig. 12. Rapid expansion reduces the role of collisions in multiple ways: (1) the densities of all particles decrease as they spread out during the expansion with densities scaling as $1/r^3$, where $r$ is the plume radius, and (2) the isentropic expansion results in more cooling (the last term in Eqs. 5 and 7), which causes a corresponding decrease in the collision rate.

As shown in Fig. 12a, a more rapid expansion ($\tau = 1$ ns) results in a greater maximum number of ions by approximately a factor of 3. The maximum value of $T_e$ is slightly higher and occurs earlier in time than in the base case (1.5 ns rather than 4 ns). However, $T_e$ decreases more rapidly due to the isentropic expansion. The maximum value of $T_g$ is much lower than in the base case because with lower densities there is less quenching of excited states which are the main cause of gas heating. There is also less energy transfer from electrons to gas heating by elastic collisions because of these lower densities.

In the case of slower expansion, with $\tau = 100$ ns, the maximum number of ions is only $3 \times 10^5$, compared to $1 \times 10^7$ in the base case. Only $3 \times 10^3$ of these survive until 10 μs. For expansion that occurs at timescales much slower than the laser pulse duration, quenching rapidly depletes excited states, reducing the electron heating rate and the ionization fraction. In much of this simulation, $T_g > T_e$. In this case, the reaction mechanism has some limitations because excitation by heavy species ($Al + Al \rightarrow Al + Al^*$) may become important but has not been included. Electron impact ionization of excited states ($e^- + Al^* \rightarrow Al^+ + e^- + e^-$) is still the main source of ions, regardless of expansion rate.

## IV. Conclusions

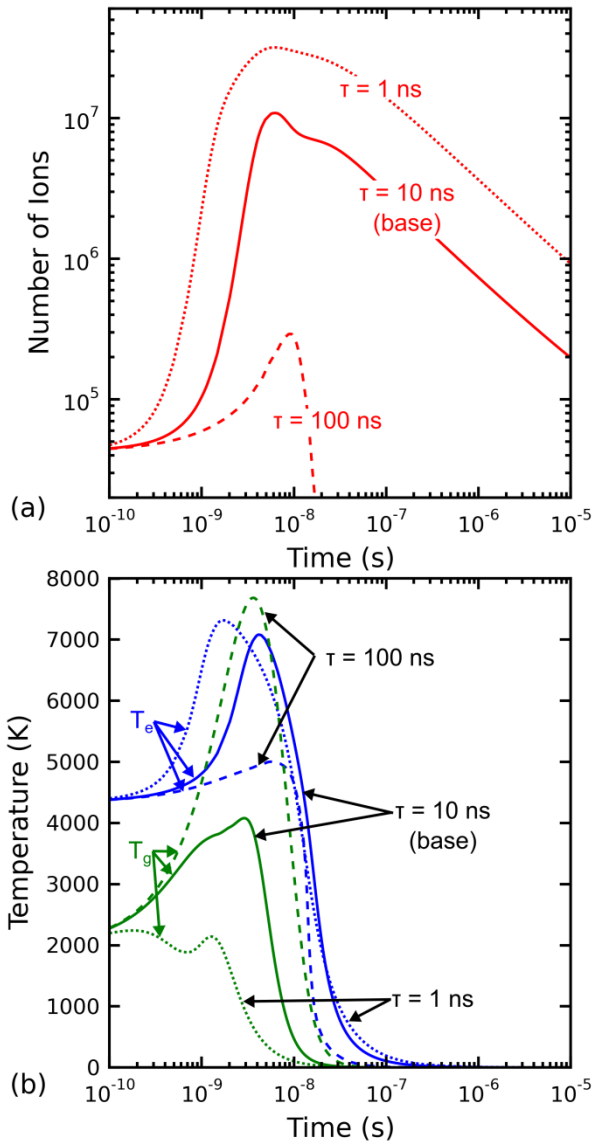


Figure 12. The effect of the characteristic expansion time, $\tau$, on the simulation results. (a) The number of $Al^+$ ions at as a function of time for $\tau = 1$, 10, and 100 ns. (b) $T_e$ and $T_g$ for $\tau = 1$, 10, and 100 ns.

In this study, a laser-produced Al plasma in vacuum was investigated using a 0-dimensional plasma chemistry model. A 248 nm laser with a pulse duration of 8 ns and a peak intensity of $1.9 \times 10^8$ W/cm$^2$ was assumed to vaporize and ionize a portion of the particle. In all of the conditions considered here, the primary ionization mechanism was electron impact ionization of excited states. The main photon absorption mechanism was direct photoexcitation by the laser to Al($y^2$D), which was made possible by pressure broadening despite being off-resonance. The population of Al($y^2$D) then underwent superelastic collisions with electrons, redistributing the energy to other excited states and heating the electrons. These hot electrons subsequently ionize Al($y^2$D) and the other excited states. The other processes considered, including photoionization of excited states, multi-photon ionization, and Penning ionization, were generally less significant than electron impact ionization of excited states by more than an order of magnitude. The excess Al($y^2$D) may be observable by time-resolved optical emission spectroscopy of the plasma. The electron temperature reached approximately 7,000 K, while the gas temperature reached 4,000 K. The electron and

gas temperatures decreased rapidly as the plasma expanded into vacuum. Most of the ions which were produced recombine by three-body recombination in the μs following the laser pulse.

Increasing the laser energy resulted in an approximately proportional increase in the total number of ions. Although many more ions are produced as the laser energy increases, the three-body recombination rate is also higher. As the particle size was increased, more Al atoms were vaporized, but this only resulted in more ion production when the plasma was still optically thin. When the plasma became optically thick to the laser light, fewer ions were produced.

Based on this study, there are several important areas of future work for better understanding ionization processes in SPAMS systems:

1. A better understanding of the timescales of expansion into vacuum would greatly improve the accuracy of these calculations.
2. The impact of an applied electric field, which is often used to collect the ions, but has not been included here, may have a significant impact on the electron temperature and decrease the three-body recombination rate.
3. Incorporation of a more realistic vaporization rate (rather than the instantaneous vaporization assumed in this work).
4. Investigation of the accuracy of the standard recombination rates near the limit of vacuum expansion and at low temperatures.
5. The effect of non-uniform heating and energy deposition by the laser, especially at early timescales where the plasma is more optically thick.

Overall, these results indicate that most of the ions recombine before they would be collected. In the design of these devices, rather than focusing on producing more ions, it may be more useful to prioritize preventing recombination. This could be done with higher collecting fields, faster expansion (potentially by tailoring laser pulses), or multiple laser pulses.

In an ideal circumstance, the number of ions collected in a SPAMS system would be proportional to the number of atoms (or molecules) of a given type in a particle, and the detection and digitization of those signals would be linear. Based on our results, the primary photon absorption mechanism in the gas phase in this system is pressure-broadened photoexcitation. This depends on a nearby transition (within a few nm), which varies significantly depending on the elements present in the plume. The fact that electron impact reactions with excited states dominate the ionization mechanisms means that any atom may be ionized, depending on its ionization energy. However, since the excited states contribute most to ionization by several orders of magnitude, the probability for direct photoexcitation of each chemical element (or molecule) in the particle must be considered as even more important than the ionization potential when interpreting data from single particle aerosol mass spectrometers that utilize ultraviolet ionization lasers. This problem may be exacerbated in SPAMS systems which have a separate laser for vaporization (usually infrared) than for ablation, because pressure-broadening is not as significant. The impact of potential resonant absorption, which more efficiently absorbs laser energy should also be considered in more detailed calibrations [6]. Alternative ionization methods, such as electron beams could also be considered to avoid this effect.

**Acknowledgements**

This work was supported by the Laboratory Directed Research and Development program at Sandia National Laboratories, a multi-mission laboratory managed and operated by National Technology and Engineering Solutions of Sandia LLC, a wholly owned subsidiary of Honeywell International Inc. for the U.S. Department of Energy's National Nuclear Security Administration under contract DE-NA0003525. This paper describes objective technical results and analysis. Any subjective views or opinions that might be expressed in the paper do not necessarily represent the views of the U.S. Department of Energy or the United States Government.

**References**


[1] C. A. Pope, N. Coleman, Z. A. Pond and R. T. Burnett, "Fine particulate air pollution and human mortality: 25+ years of cohort studies," *Environmental Research,* vol. 183, no. 108924, 2020.

[2] K. A. Pratt and K. A. Prather, "Mass spectrometry of atmospheric aerosols - recent developments and applications. Part I: Off-line mass spectrometry techniques," *Mass Spec. Rev.,* vol. 31, no. 1, (2012).

[3] J. Yang, S. Ma, B. Gao, X. Li, Y. Zhang, J. Cai, M. Li, L. Yao, B. Huang and M. Zheng, "Single particle mass spectral signatures from vehicle exhaust particles and the source apportionment of on-line PM2.5 by single particle aerosol mass spectrometry," *Sci. Total Environ.,* Vols. 593-594, p. 310, (2017).

[4] A. P. Ault, C. R. Williams, A. B. White, P. J. Neiman, J. M. Creamean, C. J. Gaston, F. M. Ralph and K. A. Prather, "Detection of Asian dust in California orographic precipitation," *J. Geophys. Res.,* vol. 116, no. D16205, (2011).

[5] E. A. Simpson, P. Campuzano-Jost, S. J. Hanna, K. M. M. Kanan, J. W. Hepburn, M. W. Blades and A. K. Bertram, "Studies of one and two component aerosols using IR/VUV single particle mass spectrometry: Insights into the vaporization process and quantitative limitations," *Phys. Chem. Chem. Phys.,* vol. 12, p. 11565, 2010.

[6] R. Gemayel, B. Temime-Roussel, N. Hayeck, A. Gandolfo, S. Hellebust, S. Gligorovski and H. Wortham, "Development of an analytical methodology for obtaining quantitative mass concentrations from LAAP-ToF-MS measurements," *Talanta,* vol. 174, pp. 715-724, 2017.

[7] D. M. Murphy, "The design of single particle laser mass spectrometers," vol. 26, pp. 150-165, (2007).

[8] K. A. Pratt and K. A. Prather, "Mass Spectrometry of Atmospheric Aerosols- Recent Developments and Applications. Part II: On-line Mass Spectrometry Techniques," *Mass Spectrometry Rev.,* vol. 31, pp. 17-48, (2012).

[9] M. S. Reinard and M. V. Johnston, "Ion Formation Mechanism in Laser Desorption Ionization of Individual Nanoparticle," *J. Am. Soc. Mass Sepctrom.,* vol. 19, pp. 389-399, (2008).

[10] Y. Oh, R. Zahaf, M. R. Zachariah and D. Lee, "Nanosecond laser induced energetic ion formation from a nanoparticle: The origin of ion detection loss in a single particle mass spect," *Jpn. J. Appl. Phys.,* vol. 53, no. 05HA10, (2014).

[11] S. K. H. Shah, J. Iqbal, P. Ahmad, M. U. Khandaker, S. Haq and M. Naeem, "Laser induced breakdown spectroscopy methods and applications: A comprehensive review," *Radiation Physics and Chemistry,* vol. 170, no. 108666, 2020.

[12] H. Shakeel, S. Arshad, S. U. Haq and A. Nadeem, "Electron temperature and density measurements of laser induced germanium plasma," *Physics of Plasmas,* vol. 23, p. 053504, (2016).

[13] N. M. Shaikh, S. Hafeez, B. Rashid and M. A. Baig, "Spectroscopic studies of laser induced aluminum plasma using fundamental, second and third harmonics of a Nd:YAG laser," *Eur. Phys. J. D,* vol. 44, p. 371, (2007).

[14] Y.-F. Lu, Z.-B. Tao and M.-H. Hong, "Characteristics of Excimer Laser Induced Plasma from an Aluminum Target," *Jpn. J. Appl. Phys.,* vol. 38, p. 2958, (1999).

[15] V. Morel, A. Bultel and G. G. Chéron, "Modeling of thermal and chemical non-equilibrium in a laser-induced aluminum plasma by means of a Collisional-Radiative model," *Spectrochimica Acta Part B,* vol. 65, p. 830, (2010).

[16] V. Morel, A. Bultel, J. Annaloro, C. Chambrelan, G. Edouard and C. Grisolia, "Dynamics of a femtosecond/picosecond laser-induced aluminum plasma out of thermodynamic equilibrium in a nitrogen background gas," *Spectrochimica Acta Part B,* Vols. 103-104, p. 112, (2015).

[17] M. A. Zawadowicz, A. Abdelmonem, C. Mohr, H. Saathoff, K. D. Froyd, D. M. Murphy, T. Leisner and D. J. Cziczo, "Single-Particle Time-of-Flight Mass Spectrometry Utilizing a Femtosecond Desorption and Ionization Laser," *Anal. Chem.,* vol. 87, pp. 12221-12229, 2015.

[18] G. Colonna, A. Casavola and M. Capitelli, "Modelling of LIBS plasma expansion," *Spectrochim. Acta B At. Spectrosc.,* vol. 56, pp. 567-586, 2001.

[19] G. Colonna, G. Pascazio and F. Bonelli, "Advanced model for the interaction of a Ti plume produced by a ns-pulsed laser in a nitrogen environment," *Spectrochim. Acta B At. Spectrosc.,* vol. 179, p. 106120, 2021.

[20] J. Passig, J. Schade, E. I. Rosewig, R. Irsig, T. Kroger-Badge, H. Czech, M. Sklorz, T. Streibel, L. Li, X. Li, Z. Zhou, H. Fallgren, J. Moldanova and R. Zimmermann, "Resonance-enhanced detection of metals in aerosols using single-particle mass spectrometry," *Atmos. Chem. Phys.,* vol. 20, pp. 7139-7152, 2020.

[21] K. Hara and K. Hanquist, "Test cases for grid-based direct kinetic modeling of plasma flows," *Plasma Sources Sci. Technol.,* vol. 27, no. 065004, 2018.

[22] M. Surendra, D. B. Graves and G. M. Jellum, "Self-consistent model of a direct-current glow discharge: Treatment of fast electrons," *Phys. Rev. A,* vol. 41, no. 2, p. 1112, (1990).

[23] M. Gryzinski, "Classical theory of atomic collisions I. Theory of inelastic collisons," *Phys. Rev.,* vol. 138, no. 2A, (1965).

[24] M. A. Lieberman and A. J. Lichtenberg, Principles of Plasma Discharges and Materials Processing, Second Edition ed., Hoboken, NJ: John Wiley & Sons, Inc., 2005.

[25] N. Konjevic, "Plasma broadening and shifting of non-hydrogenic spectral lines: present status and applications," *Phys. Rep.,* vol. 316, no. 339, (1999).

[26] Y.-K. Kim and P. M. Stone, "Ionization of boron, aluminum, gallium, and indium by electron impact," *Phys. Rev. A,* vol. 64, no. 052707, (2001).

[27] Y. I. Ryabikh and I. I. Fabrikant, "Partial-wave analysis of low-energy electron scattering by aluminium atoms," *J. Phys. B: At. Mol. Phys.,* vol. 14, no. 349, (1981).

[28] A. Bogaerts, K. A. Temelkov, N. K. Vuchkov and R. Gijbels, "Calculation of rate constants for asymmetric charge transfer, and their effect on relative sensitivity factors in glow discharge mass spectrometry," *Spectrochemica Acta Part B,* vol. 62, no. 325, (2007).

[29] N. R. Badnell, "Radiative recombination data for modeling finite-density plasmas," *Astrophys. J. Suppl. Series,* vol. 167, pp. 334-342, (2006).

[30] Z. Altun, A. Yumak, I. Yavuz, N. R. Badnell, S. D. Lock and M. S. Pindzola, "Dielectronic recombination data for dynamic finite-density plasmas," *Astron. and Astrophys.,* vol. 474, pp. 1051-1059, (2007).

[31] Y. Hahn, "Plasma density effects on the three-body recombination rate coefficients," *Phys. Lett. A,* vol. 231, no. 82, (1997).

[32] C. D. Bie, J. van Dijk and A. Bogaerts, "CO2 Hydrogenation in a Dielectric Barrier Discharge Plasma Revealed," *J. Phys. Chem. C,* vol. 120, no. 25210, 2016.

[33] "NIST Atomic Spectra Database," [Online]. Available: https://www.nist.gov/pml/atomic-spectra-database.

[34] N. M. Shaikh, S. Hafeez, B. Rashid and M. A. Baig, "Spectroscopic studies of laser induced aluminum plasma using fundamental, second and third harmonics of a Nd:YAG laser," *Eur. Phys. J. D,* vol. 44, pp. 371-379, (2007).

[35] Y. B. Zel'dovich and Y. P. Raizer, Physics of Shock Waves and High-Temperature Hydrodynamic Phenomena, New York: Academic, 1967.

[36] J. Cabalo, A. Zelenyuk, T. Baer and R. E. Miller, "Two-color laser induced evaporation dynamics of liquid aerosols proved by time-of-flight mass spectrometry," *Aerosol Sci. Technol. ,* vol. 33, pp. 3-19, 2000.

[37] "NIST Chemistry WebBook," 2018. [Online]. Available: https://webbook.nist.gov/cgi/inchi/InChI%3D1S/Al. [Accessed 12 July 2021].

[38] D. R. Lide, CRC Handbook of Chemistry and Physics, Boca Raton, FL: CRC Press, 2003.

[39] J. A. Dean, Lange's Handbook of Chemistry, 15 ed., New York, NY: McGraw-Hill, 1999.

[40] R. A. Paquin, "Properties of Metals," in *Handbook of Optics*, vol. II, M. Bass, E. W. Van Stryland, D. R. Williams and W. L. Wolfe, Eds., McGraw-Hill, 1995.

[41] R. G. Pinnick, A. Biswas, R. L. Armstrong, S. G. Jennings, J. D. Pendleton and G. Fernandez, "Micron-sized droplets irradiated with a pulsed CO2 laser: measurement of explosion and breakdown thresholds," *Applied Optics,* vol. 27, no. 7, 1990.

[42] D. Marla, U. V. Bhandarkar and S. S. Joshi, "A model of laser ablation with temprature-dependent material properties, vaporization, phase explosion and plasma shielding," *Appl. Phys. A,* vol. 116, p. 273, (2014).

[43] K. Yamada, I. Wantanabe, T. Kubo, M. Umeno, K. Yoshii and H. Kawabe, "Investigations of holes machined by laser beam on Al and Cr thin films," *J. Appl. Phys.,* vol. 53, no. 3231, (1982).

[44] G. Bird, Molecular Gas Dynamics and the Direct Simulation of Gas Flows, Oxford: Oxford University Press, 2005.

[45] T. Soga, "Spherical source flow expansion of single monatomic gasses into vacuum," Institute of Space and Aeronautical Science, Tokyo, 1972.

[46] N. Farid, S. S. Harilal, H. Ding and A. Hassanein, "Emission features and expansion dynamics of nanosecond laser ablation plumes at different ambient pressures," *J. Appl. Phys.,* vol. 115, no. 033107, (2014).

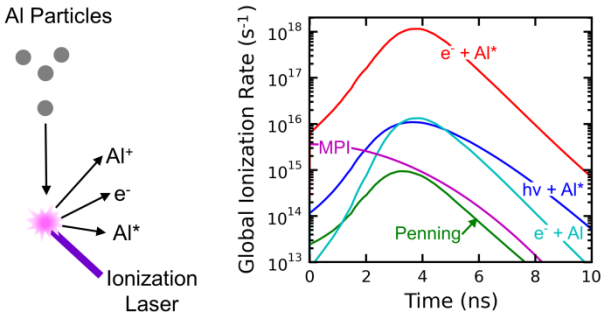


Graphical abstract.